The Canadian Mineralogist
Vol. 51, pp. 785-800 (2013)
DOI: 10.3749/canmin.51.5.785

A COMBINED GEOCHEMICAL AND GEOCHRONOLOGICAL INVESTIGATION OF NIOCALITE FROM THE OKA CARBONATITE COMPLEX, CANADA

WEI CHEN[§], ANTONIO SIMONETTI, AND PETER C. BURNS[*]

Department of Civil & Environmental Engineering & Earth Sciences, 156 Fitzpatrick Hall, University of Notre Dame, Notre Dame IN, 46556 USA

ABSTRACT

This study is the first to report a detailed geochemical investigation and *in situ* U-Pb ages for niocalite, which occurs within carbonatite from the Bond Zone area of the Oka Carbonatite Complex (Canada). Niocalite is a Nb-disilicate member of the låvenite–cuspidine group. The major element composition of the niocalite studied here is relatively homogeneous with the average formula of: $(Na_{0.34}Fe_{0.06}Mn_{0.19}Mg_{0.09}Ca_{13.40}REE_{0.15}Ti_{0.02})_{\Sigma 14.25}Nb_{2.12}Ta_{0.06}(Si_2O_7)_4O_{7.65}F_{2.44}$. Niocalite is enriched in minor and trace elements [*i.e.*, Ta, Ti, and rare earth elements (REEs) up to 4.35 wt.%], with double- and triple-valenced elements (*i.e.*, Sr, Y, REEs) substituting at different Ca-occupied lattice sites. The chondrite-normalized REE patterns for niocalite are LREE-enriched (~10^4 times chondrite) and negatively sloped. In addition, niocalite has higher HREE contents compared to those for co-existing apatite from the identical carbonatite sample. This result is expected based on bond valence data because of differing cation sizes. *In situ* U-Pb ages for niocalite from three carbonatite samples obtained by LA-ICP-MS define a wide range of ages, between ~111 and ~133 Ma. Niocalite from one carbonatite sample yields a bimodal distribution with weighted mean $^{206}Pb/^{238}U$ ages of 110.1 ± 5.0 Ma and 133.2 ± 6.1 Ma, and overlap those of co-existing apatite for the same sample. Two other samples of carbonatite yield weighted mean $^{206}Pb/^{238}U$ ages of 110.6 ± 1.2 Ma and 115.0 ± 1.9 Ma. The geochronological data for niocalite reported here suggests a protracted petrogenetic history for Oka, which corroborates the relatively large range of ages (~20 Myr) previously determined for apatite from the Oka complex. *In situ* $^{87}Sr/^{86}Sr$ isotope ratios for niocalite obtained by LA-MC-ICP-MS are variable and range between 0.70314 (±7) and 0.70343 (±8). Based on the combined U-Pb ages, major and trace element abundances, and Sr isotope ratios, the history of niocalite formation cannot be attributed to either simple closed-system fractional crystallization or carbonate-silicate liquid immiscibility. Rather, these are consistent with periodic carbonatite melt derivation from a heterogeneous mantle source, and suggest that some of niocalite investigated here represent cognate crystals.

INTRODUCTION

Niocalite is a monoclinic disilicate mineral belonging to the låvenite–cuspidine group, and is a rare accessory mineral in carbonatite, nepheline syenite, and metamorphosed carbonatite (Bellezza *et al.* 2004, Casillas *et al.* 2008). The minerals belonging to the låvenite–cuspidine group are important repositories for high field strength elements (HFSEs), specifically Nb, Zr, and Ti (Chakhmouradian *et al.* 2008). The general chemical formula for this group is $M_{16}(Si_2O_7)_4(O,OH,F)_8$ (Bellezza *et al.* 2004, Merlino & Perchiazzi 1988), where M represents sites for cations with coordination number from VI to VIII; this includes high-charge and small-radius cations (*e.g.*, Nb^{5+}, Zr^{4+}, Ti^{4+}, REE^{3+}, Mn^{2+}, Fe^{2+}), and low-charge and large-radius Ca^{2+} and Na^{+} cations. Detailed chemical formulae of the låvenite–cuspidine group minerals are listed in Bellezza *et al.* (2004). The crystal structure for this group consists of a wall of edge-sharing $Ca(O,F)_n$ polyhedra ('octahedral') parallel to the c-axis and the diorthosilicate groups, which are corner-linked to the walls (Merlino & Perchiazzi 1988).

Niocalite [essentially $Ca_{14}Nb_2(Si_2O_7)_4O_6F_2$] has been described from only four localities world-wide: Oka, Canada (Nickel 1956, Nickel *et al.* 1958); the Oldoinyo Lengai volcano, Tanzania (Mitchell &Belton 2004); Kaiserstuhl, Germany (Keller *et al.* 1995); and the Basal Complex of Fuerteventura, Canary Islands, Spain (Casillas *et al.* 2008). At Oldoinyo Lengai, compositions for the sodian cuspidine–niobian cuspidine–niocalite solid-solution series were reported by Mitchell & Belton (2004). Casillas *et al.* (2008) described the cuspidine–niocalite–baghdadite solid solutions in the metacarbonatites from the Basal Complex of Fuerteventura. At Kaiserstuhl, niocalite occurs with wöhlerite in the calcite-silicate rocks (Keller *et al.* 1995), whereas niocalite at Oka occurs

§ *Corresponding author*: wchen2@nd.edu
* *E-mail address*: pburns@nd.edu

as prismatic crystals and is typically associated with calcite and apatite in coarse-grained carbonatite within the Bond Zone area (Fig.1).

Limited trace element data has been reported to date for niocalite belonging to the låvenite–cuspidine group; however, Fleet & Pan (1995) predicted suitable sites for REE substitution in cuspidine. In addition, significant amounts of Y and heavy REEs (HREEs) in hiortdahlite, a calc-silicate zirconate, were reported by Aarden & Gittins (1974). Hence, a detailed study of the trace element compositions of the låvenite–cuspidine group minerals (*e.g.*, niocalite) is lacking, along with their distribution within the crystal structure.

Due to their enrichment in trace elements (especially Sr, U, Pb), niocalite and associated group minerals are potential candidates for geochronological and isotopic studies. Kapustin (1980) concluded that niocalite usually crystallizes early within phosphorus-free carbonatites, and that it is ultimately replaced by lattrapite or pyrochlore; the latter possibly formed during emplacement of second stage carbonatites and accompanied by co-crystallization of apatite. Thus, this formational model can be evaluated here by comparing *in situ* U-Pb ages obtained from individual niocalite and co-existing apatite crystals from the same whole rock sample.

This paper aims to investigate the structure, major and trace element abundances, Sr isotope compositions, and crystallization ages for niocalite from the Oka Carbonatite Complex, examining, in particular, the role of niobium incorporation within the walls of the Nb-rich cuspidine crystal structure based on trace element substitution schemes. Lastly, the combined Sr isotope measurements and *in situ* U-Pb ages obtained for niocalite will be used to help determine the crystallization history of the host carbonatite melt, and the chemical nature of its corresponding mantle source.

Niocalite occurrence and mineral paragenesis

The Monteregian Igneous Province (MIP) consists of nine alkaline plutons and associated dikes emplaced within southern Québec (Fig. 1A), of which Oka is the sole carbonatite complex (Eby 1984, Foland *et al.* 1986). Oka represents the most westerly alkaline intrusion of the MIP (Gold 1972, Gold *et al.* 1986; Fig. 1B), and Gold *et al.* (1986) provide a detailed geological description of the complex. The complex was mined for Nb (pyrochlore) for several years, with the St. Lawrence Columbium, Bond Zone, and NIOCAN deposits constituting the three main occurrences for niobium (Fig. 1B; Gold *et al.* 1986, Zurevinski & Mitchell 2004). The three coarse-grained carbonatite samples investigated in this study (Oka153, Oka203, Oka206) were retrieved from the Bond Zone area. The niocalite within these calciocarbonatites occurs as prismatic crystals and is randomly oriented amongst the coexisting apatite and calcite (Fig. 2). Other minerals associated with the carbonatite from this area include clinopyroxene, magnetite, biotite, and other Nb-bearing minerals, pyrochlore and Nb-perovskite.

METHODS

Single Crystal X-ray Diffraction

A single niocalite crystal devoid of inclusions was selected, fixed to a tapered glass fiber, and mounted on a Bruker three-circle diffractometer equipped with an APEX II CCD detector and graphite-monochromatized Mo$K\alpha$ radiation at the University of Notre Dame. Data collection utilized frame widths of 0.5° in ω-scan. The Bruker program APEX II was used to correct for Lorentz, polarization, and background effects. Absorption corrections were applied using the program SADABS, and structures were solved and refined using the Bruker SHELXTL v6.12 software.

Electron Microprobe Analysis (EMPA)

Identification of textures and minerals within petrographic thin sections (~75 to 100 μm thick) was investigated by optical microscopy, and back-scattered electron (BSE) imaging was carried out by electron microprobe analysis (EMPA). Preliminary evaluation of mineral compositions was determined by scanning electron microscope (SEM) using energy dispersive spectroscopy (EDS) at the University of Notre Dame Integrated Imaging Facility (NDIIF). Semi-quantitative EDS analyses were obtained for certain minerals with increased integration time (120 to 180s). Fully quantitative major and minor element compositions were subsequently obtained by wavelength-dispersive spectroscopy (WDS) analysis using a Cameca SX50 electron microprobe at the University of Chicago (Table 1). EMP analyses were conducted using a 15 kV accelerating potential and 30 nA incident current, and the natural and synthetic mineral and glass standards employed for calibration purposes were: natural olivine (for Fe, Mn, Mg, and Si), natural albite (for Na), synthetic glass of anorthite composition (for Al, Ca), natural microcline (for K), synthetic CaF_2 (for F), synthetic TiO_2 (for Ti), synthetic REE3 (for Ce), synthetic NB (for Nb), and synthetic TA (for Ta). Peak counting times for these elements were (element, time in seconds): Si, 10; Ca, 10; Nb, 10; Fe, 20; Mn, 20; Ce, 30; Ta, 40; F, 20; Na, 20; Mg, 20; Al, 20; K, 30; Ti, 40.

Trace element analysis via LA-ICP-MS

In situ trace element analyses of individual niocalite grains (Table 2) were obtained using a New Wave UP213 nm laser ablation (LA) system coupled to a Thermo-Finnigan Element2 sector field high-resolu-

tion inductively coupled plasma mass spectrometer (HR-ICP-MS) housed within MITERAC, University of Notre Dame. Instrument parameters and conditions are similar to those described in Chen & Simonetti (2013). A NIST SRM 610 glass wafer was used as the external standard and Ca (CaO wt.% contents from EMPA) as the internal standard to monitor ionization efficiency related to plasma conditions and instrumental drift. Niocalite and standards were ablated with a 25 μm spot size, 5 Hz repetition rate, and corresponding energy density of ~10 J/cm^2. Data reduction, which included determination of elemental concentrations, mean detection limits, and associated uncertainties, was conducted using GLITTER laser ablation software (Van Achterbergh *et al*. 2001).

U-Pb geochronology via LA-ICP-MS

The instrument configuration described above for *in situ* trace element analysis is identical to the one used for the *in situ* U-Pb age determinations reported here by LA-ICP-MS. Zircon BR266 was selected as the matrix-matched external standard given its similar SiO_2 content compared to niocalite, and because it is a standard well-characterized by thermal ionization mass spectrometry (TIMS; Stern & Amelin 2003) and LA-MC-ICP-MS (Simonetti *et al*. 2005) methods; reference $^{207}Pb/^{206}Pb$, $^{207}Pb/^{235}U$, $^{206}Pb/^{238}U$ ratios for BR266 are 0.05888, 0.7354, and 0.09058, respectively. Figure 3 depicts typical time-resolved LA-ICP-MS analyses for zircon standard BR266 and for an individual analysis of niocalite (Sample Oka203), and these display coherent and similar patterns with negligible down-hole U/Pb fractionation. Each set of 12–16 unknown analyses of niocalite was bracketed with 5 analyses of the BR266 zircon standard. Individual niocalite grains and zircon standard were lasered in raster mode using areas of 60 × 60 μm, repetition rate of 5 Hz, and corresponding fluence of ~ 8J/cm^2. The following ion signals were measured: ^{202}Hg, ^{204}(Pb+Hg), ^{206}Pb, ^{207}Pb, ^{208}Pb, ^{235}U,

TABLE 1. MAJOR AND MINOR ELEMENT COMPOSITIONS OF NIOCALITE FROM OKA

	Oka206 (*n* = 21)	2σ	Oka203 (*n* = 20)	2σ	Oka153 (*n* = 4)	2σ
wt.%						
FeO	0.30	0.03	0.20	0.05	0.29	0.10
MnO	0.82	0.02	0.66	0.09	0.98	0.13
MgO	0.24	0.01	0.19	0.04	0.21	0.05
CaO	45.74	0.15	45.87	0.23	45.73	0.11
Al_2O_3	0.006	0.003	0.003	0.002	0.004	0.004
SiO_2	29.39	0.14	29.40	0.12	29.10	0.47
Nb_2O_5	16.88	0.14	17.04	0.11	17.70	0.37
Ta_2O_5	0.89	0.07	0.48	0.08	0.16	0.21
TiO_2	0.13	0.01	0.10	0.01	0.09	0.03
REE_2O_3	1.37	0.09	1.36	0.14	1.92	0.18
Na_2O	0.60	0.02	0.66	0.03	0.70	0.05
K_2O	0.006	0.002	0.004	0.002	0.014	0.004
F	2.87	0.09	2.83	0.11	2.78	0.37
SUM	99.24		98.79		99.67	
apfu						
Fe^{2+}	0.0041	0.0004	0.0027	0.0007	0.0041	0.0013
Mn	0.0116	0.0003	0.0093	0.0012	0.0137	0.0019
Mg	0.0059	0.0004	0.0047	0.0009	0.0052	0.0013
Ca	0.8157	0.0026	0.8180	0.0041	0.8155	0.0019
Al	0.0001	0.0001	0.0001	0.0000	0.0001	0.0001
Si	0.4891	0.0023	0.4892	0.0020	0.4843	0.0079
Nb	0.1270	0.0011	0.1282	0.0008	0.1332	0.0028
Ta	0.0068	0.0005	0.0037	0.0006	0.0013	0.0016
Ti	0.0017	0.0001	0.0012	0.0001	0.0011	0.0004
REE	0.0083	0.0005	0.0083	0.0008	0.0117	0.0011
Na	0.0194	0.0005	0.0212	0.0010	0.0225	0.0016
K	0.0001	0.0000	0.0001	0.0000	0.0003	0.0001
F	0.1509	0.0050	0.1487	0.0060	0.1464	0.0197
O	2.1758	0.0139	2.1686	0.0166	2.1743	0.0364
F+O	2.3268	0.0189	2.3173	0.0226	2.3207	0.0562

Note: Detection limit varied within the range of 0.02 to 0.04 wt.%, and the analytical uncertainties are within 5%.

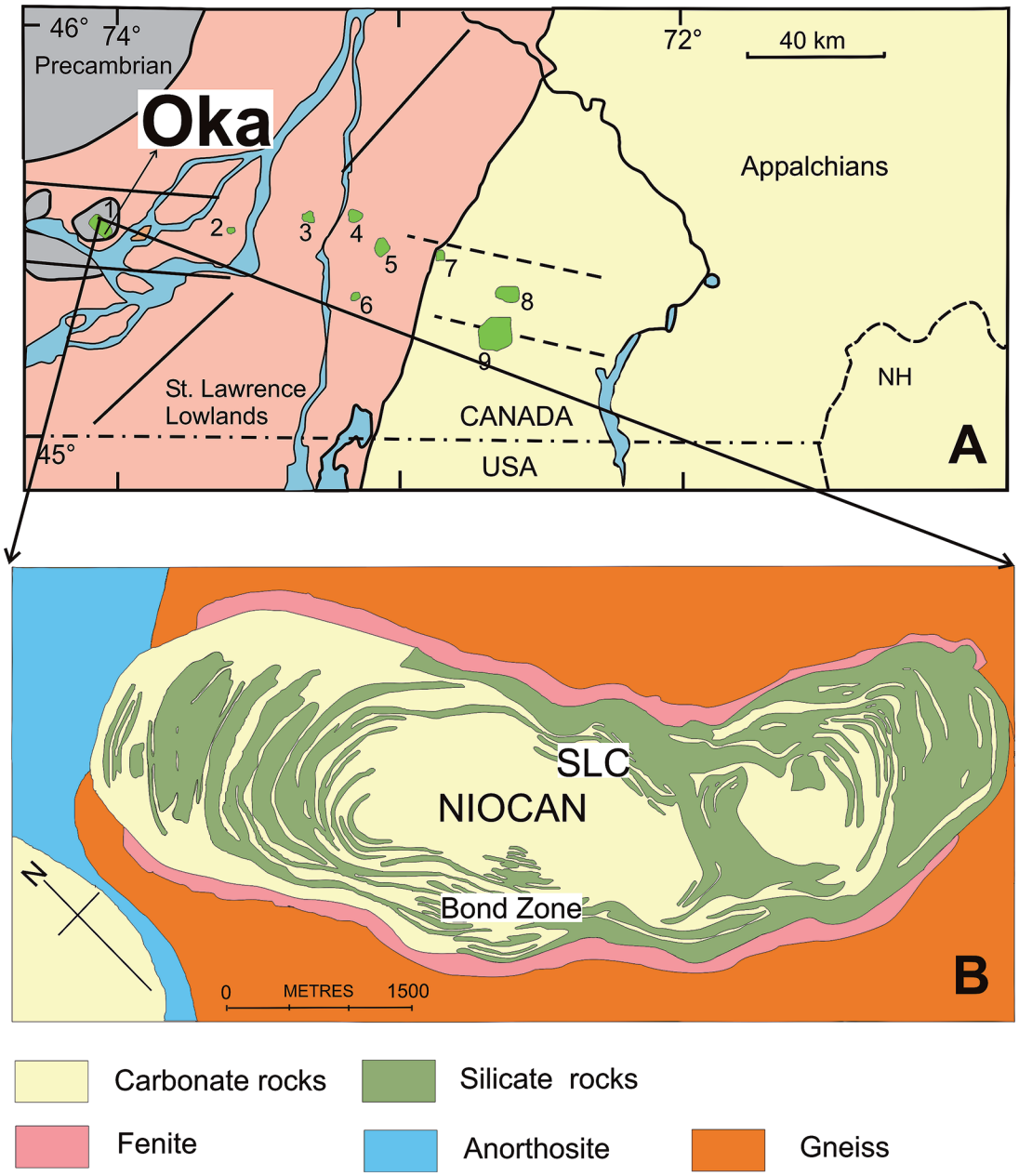

FIG. 1. Geological map of the Monteregian Igneous Province -MIP (A; after Foland *et al.* 1986) and Oka carbonatite complex (B; after Gold *et al.* 1986). (A) Intrusions identified are: 1- Oka; 2-Royal; 3- St. Hilaire; 5- Rougemont; 6- Johnson; 7- Yamaska; 8- Shefford; 9- Brome. (B) Shown are locations of the Nb deposits within the Oka carbonatite complex: SLC (St. Lawrence Columbium), NIOCAN, and Bond Zone; the latter is the type locality for niocalite.

and ^{238}U. Uncertainties associated with individual analyses, which includes propagation of errors from individual analysis measurements (based on counting statistics) and relative standard deviation associated with repeated measurements of the BR266 zircon standard, were determined using a quadratic equation

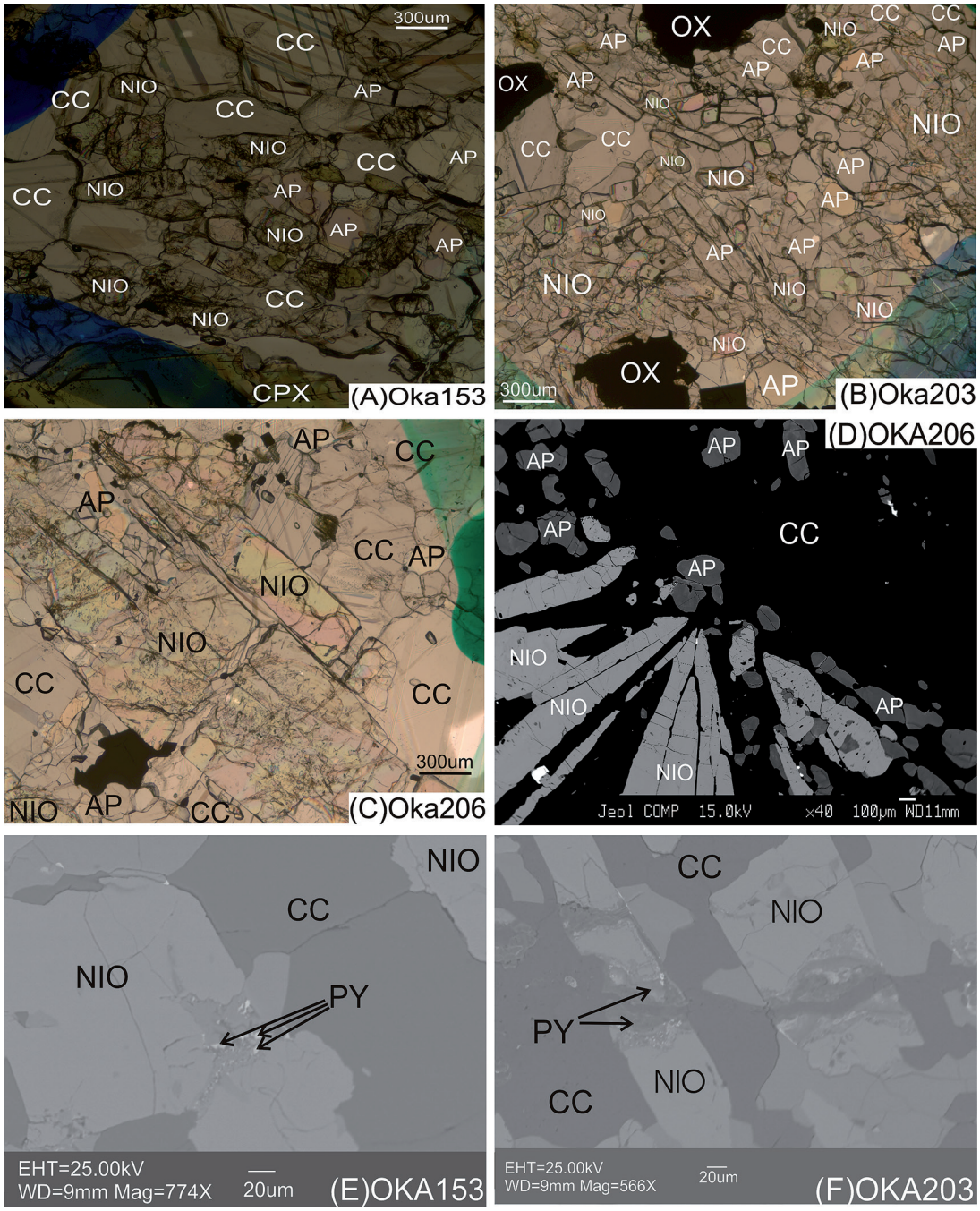

FIG. 2. Photomicrographs depicting occurrences of niocalite within petrographic thin sections of carbonatite. (A) Sample Oka153, niocalite (NIO) occurs with apatite (AP), calcite (CC), and clinopyroxene (CPX); (B) Sample Oka203, randomly oriented niocalite crystals together with apatite, calcite, and oxides (OX); (C) Sample Oka206, large niocalite crystals co-existing with apatite and calcite; (D) Back-scattered electron (BSE) image of sample Oka206 exhibiting oriented, needle-like niocalite crystals; (E) BSE image of sample Oka153 illustrating resorbed niocalite with pyrochlore (PY) inclusions; (F) BSE image of sample Oka203 shows presence of secondary pyrochlore formed as a result of late-stage hydrothermal activity – see text for details.

TABLE 2. TRACE ELEMENT COMPOSITIONS OF NIOCALITE FROM OKA

	Oka206 (*n* = 21)	2σ	Oka203 (*n* = 20)	2σ	Oka153 (*n* = 4)	2σ	Oka203_AP (*n* = 20)	2σ
Sr	2677	206	2570	70	2598	72	9337	479
Y	1007	76	514	30	1327	87	504	36
Zr	2838	451	3491	267	451	128	21	4.95
Ba	37	7.40	58	26	70	14	165	5.65
La	1895	103	1816	38	2761	61	11884	402
Ce	4564	279	4488	82	6171	192	21673	527
Pr	496	34	500	8.72	699	16	1975	44
Nd	1815	141	1801	36	2705	18	5910	187
Sm	285	26	260	6.63	444	11	551	22
Eu	92	8.22	75	1.69	129	2.40	149	4.02
Gd	194	18	158	6.14	302	9.14	302	16
Tb	30	2.69	21	0.94	45	2.12	30	1.28
Dy	168	14	99	4.78	234	9.01	126	6.37
Ho	34	2.54	17	0.92	45	2.74	19	1.42
Er	100	7.41	47	2.71	131	11	42	3.44
Tm	16	1.12	6.80	0.42	19	1.34	4.47	0.39
Yb	128	8.26	52	3.11	142	11	24	2.72
Lu	18	1.30	7.35	0.48	21	1.79	2.76	0.32
Hf	6.66	1.29	9.50	0.94	1.00	0.31	0.07	0.04
Pb	6.78	5.50	3.12	0.44	4.70	1.70	2.33	0.34
Th	2.49	0.77	13	0.85	3.71	1.18	51	4.71
U	411	95	305	32	141	21	153	22
La/Yb	10		24		13		337	

Notes: The concentrations of elements are presented in ppm; the analytical uncertainties for each element are within 4%.

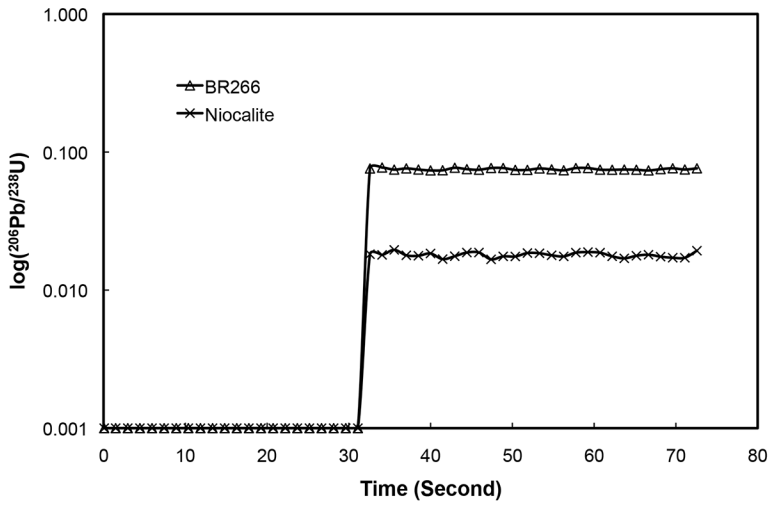

FIG. 3. Time-resolved plot [time *versus* log(^{206}Pb/^{238}U)] illustrating typical LA-ICP-MS analyses of BR266 zircon standard and niocalite from sample Oka203.

TABLE 3. Sr ISOTOPIC RATIOS FOR CORAL STANDARD AND NIOCALITE

Sample	Anal. #	Sr (ppm)	$^{87}Sr/^{86}Sr$	2σ	$^{84}Sr/^{86}Sr$	2σ	$^{84}Sr/^{88}Sr$	2σ	^{88}Sr (V)
Coral	COR1		0.70914	0.00003	0.05615	0.000078	0.00670	0.000009	13.4
	COR2		0.70914	0.00002	0.05644	0.000040	0.00674	0.000004	16.7
	COR3		0.70917	0.00002	0.05669	0.000047	0.00678	0.000006	15.0
Oka203	NIO1	2941	0.70314	0.00010	0.05678	0.000387	0.00678	0.000046	2.7
	NIO3	2493	0.70326	0.00009	0.05641	0.000294	0.00673	0.000035	3.3
	NIO5	2464	0.70338	0.00010	0.05698	0.000273	0.00680	0.000034	3.4
Oka206	NIO1_2	2588	0.70318	0.00005	0.05674	0.000099	0.00677	0.000012	3.8
	NIO1_4	2591	0.70324	0.00004	0.05647	0.000075	0.00674	0.000009	6.2
	NIO5	2764	0.70343	0.00008	0.05674	0.000081	0.00678	0.000010	3.2
Oka153	NIO1	2703	0.70314	0.00007	0.05788	0.000155	0.00686	0.00002	2.1
	NIO3	2582	0.70340	0.00006	0.05659	0.000063	0.00675	0.000007	3.1

(*e.g.*, Horstwood *et al.* 2003, Simonetti *et al.* 2005, Storey *et al.* 2006). Isoplot v3.0 was used for plotting of Tera-Wasserburg diagrams and Concordia lower intercept and $^{206}Pb/^{238}U$ weighted mean age calculations (Ludwig 2003).

In situ Sr isotope ratios via LA-MC-ICP-MS

In situ Sr isotope ratios of niocalite (Table 3) were determined using a New Wave Research (NWR193) excimer laser ablation system coupled to a Nu PlasmaII MC-ICP-MS instrument at the MITERAC facility, University of Notre Dame. *In situ* Sr isotope measurements involve correction of critical spectral interferences that include Kr, Rb, and doubly charged REEs (Ramos *et al.* 2004, Paton *et al.* 2007). Hence, the following corrections were applied: ^{85}Rb ion signal is monitored to correct for the ^{87}Rb isobaric overlap on mass ^{87}Sr; elimination of ^{84}Kr, ^{86}Kr, and ArO_3 interferences with a 30s on-peak baseline measurement prior to laser ablation; and monitoring of doubly charged REE ion signals at half-mass positions (masses 83 for $^{166}Er^{2+}$ and 86.5 for $^{173}Yb^{2+}$) with additional Faraday detectors (Ramos *et al.* 2004, Paton *et al.* 2007). The measured doubly-charged REE ($^{170}Er^{2+}$ and $^{170}Yb^{2+}$) ion signals were applied to the correction of the ^{85}Rb ion signal. A modern-day coral (Indian Ocean) served as an external, in-house standard, which was well characterized by ID-TIMS (isotope dilution – thermal ionization mass spectrometry; Bizzarro *et al.* 2003), which is used to validate and assess the accuracy of the analytical method employed here. The coral standard and niocalite grains were analyzed using a 75 μm spot size, 7 Hz repetition rate, and an energy density ~11 J/cm^2. The average $^{87}Sr/^{86}Sr$ value obtained for the coral standard is 0.70915 ± 0.00003 based on 3 measurements (Table 3), and is indistinguishable (given uncertainties) compared to the corresponding TIMS value of 0.70910 ± 0.00002 (Bizzarro *et al.* 2003).

RESULTS

Single crystal X-ray diffraction

X-ray diffraction analysis of niocalite indicates that it is monoclinic with, a = 7.37 Å, b = 10.43 Å, c = 10.85 Å, α = 90.00°, β = 109.84°, γ = 90.00°, and the crystal structure parameters are similar to those reported for niocalite by Mellini (1982).

Major and minor element compositions

The major element composition of niocalite from Oka is similar to that reported by Nickel *et al.* (1958) and Mellini (1982). The calculated chemical formula for niocalite (assuming eight silicon atoms per unit cell) based on the cerium abundances obtained by EMPA and trace element determinations obtained by LA-ICP-MS can be expressed as: $(Na_{0.34}Fe_{0.06}Mn_{0.19}Mg_{0.09}Ca_{13.40}REE_{0.15}Ti_{0.02})_{\Sigma 14.25}Nb_{2.12}Ta_{0.06}(Si_2O_7)_4O_{7.65}F_{2.44}$.

Figure 4 illustrates several elemental variation diagrams and these clearly indicate negative correlations between the abundances of calcium and iron, magnesium, and manganese, respectively; the latter result indicates that manganese can be regarded as 2+ charged ion in niocalite. These inverse correlations suggest the following substitution schemes: $Fe^{2+} \leftrightarrow Ca^{2+}$; $Mg^{2+} \leftrightarrow Ca^{2+}$; $Mn^{2+} \leftrightarrow Ca^{2+}$.

Trace element systematics

The trace element abundances of niocalite are listed in Table 2. Due to the various sites (and respective bond distances) occupied by Ca and Nb within niocalite (Table 4), substitutions occur and result in the incorporation of a variety of trace elements; the substitution schemes are discussed later. Compared to the trace element compositions of apatite from Oka for the same sample (Chen & Simonetti 2013), the abundances of

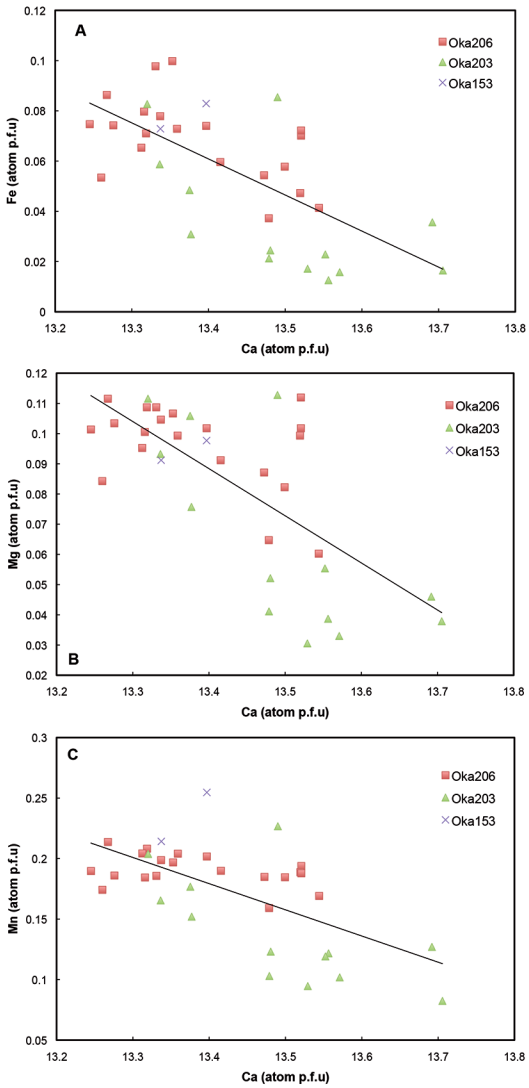

FIG. 4. Plots of major and minor element abundances (in atoms per formula unit with Si = 8) for niocalite from the Oka carbonatite complex. (A) Fe *versus* Ca; (B) Mg *versus* Ca; (C) Mn *versus* Ca.

Sr, Y, Zr, Hf, Th, U, and HREEs are higher in niocalite (Table 2). Chondrite-normalized REE patterns for niocalite are negatively sloped and light REE- (LREE) enriched (Fig. 5); the patterns are less steep, with relatively flat HREE-normalized values compared to the average normalized pattern for apatite (*e.g.*, sample Oka203). $(La/Yb)_N$ ratios vary from 10 to 24 times chondrite in niocalite and the corresponding average ratio is 337 for apatite from Oka203. In addition, the LREE-normalized values for niocalite are fairly consistent, whereas those for the HREEs are variable (Fig. 5).

In situ U-Pb ages for niocalite

In situ U-Pb dating of niocalite must effectively deal with the presence of common Pb, as is the case with apatite (*e.g.*, Chew *et al.* 2011, Chen & Simonetti 2013), titanite (*e.g.*, Banerjee *et al.* 2007, Fliegel *et al.* 2010, Simonetti *et al.* 2006, Storey *et al.* 2006, Simonetti *et al.* 2008), and perovskite (*e.g.*, Cox & Wilton 2006, Simonetti *et al.* 2008). Cox & Wilton (2006) outlined the methods (graphical and equations) for correction of the common Pb component, in particular for perovskite, which is typically characterized by high Th/U ratios. Furthermore, the common Pb may be corrected effectively by using a matrix-matched standard for the monitoring and correction of the instrumental Pb-U fractionation (*e.g.*, Batumike *et al.* 2008, Tappe & Simonetti 2012). For laser ablation-ICP-MS analyses, measurement of the ^{204}Pb ion signal is hampered by the presence of the ^{204}Hg contaminant present in the Argon plasma gas supply. As with the *in situ* dating of apatite (Chew *et al.* 2011, Chen & Simonetti 2013), titanite (Banerjee *et al.* 2007, Fliegel *et al.* 2010, Simonetti *et al.* 2006, Simonetti *et al.* 2008, Storey *et al.* 2006), and perovskite (Batumike *et al.* 2008, Cox & Wilton 2006, Simonetti *et al.* 2008, Wu *et al.* 2010), the ^{207}Pb/^{206}Pb-method (*i.e.*, employing the Tera-Wasserburg diagram) is also suitable for U-Pb dating of niocalite and is adopted in this study.

The U-Pb isotope data for niocalite are listed in Table 5, and the Tera-Wasserburg and weighted mean ^{206}Pb/^{238}U age diagrams are shown in Figure 6. In the Tera-Wasserburg plot, the y-intercept of the best-fit linear regression (as calculated by IsoPlot) represents the ^{207}Pb/^{206}Pb composition of the common Pb component (Fig. 6), the idea being that the latter is devoid of any U (or Th) and therefore its ^{238}U/^{206}Pb value is zero. The crystallization age of the mineral is given by the lower intersection of the regression line and the Concordia curve, which represents the isotopic composition of the "radiogenic" component

TABLE 4. BOND DISTANCES (Å) AND BOND STRENGTH BALANCE (V.U.) IN NIOCALITE (MELLINI 1982)

	Bond distance (Å)	Bond strength balance (v.u.)	Ligand
Ca1	2.456	1.89	O
Ca2	2.362	1.90	O
Ca3	2.499	1.72	O, F
Ca4	2.411	2.30	O, F
Nb	2.048	4.44	O
Ca6	2.523	1.91	O, F
Ca7	2.580	1.81	O, F
Ca8	2.374	1.85	O

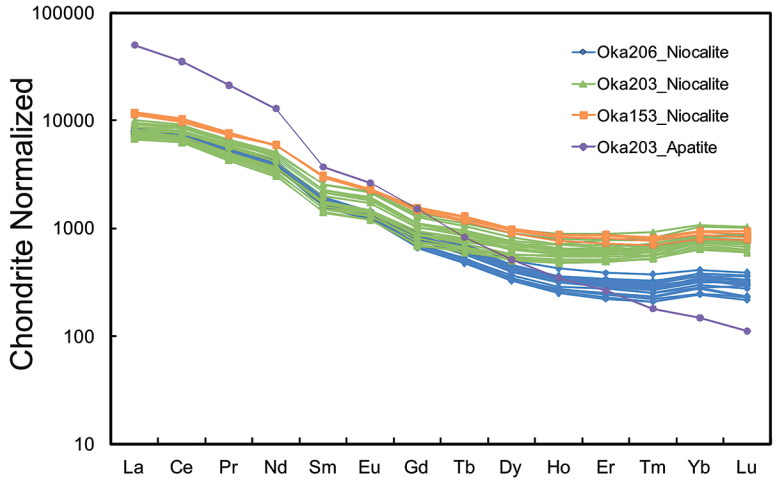

FIG. 5. Chondrite-normalized REE patterns for average niocalite compositions from samples investigated here. Average REE-normalized pattern for apatite from sample Oka203 (Table 2; Chen & Simonetti 2013) is shown for comparison. Chondrite REE concentrations are from McDonough & Sun (1995).

(Fig. 6). Two distinct scenarios are shown in Figure 6. In the first case, the individual laser ablation analyses of niocalite are characterized by variable contents of radiogenic and common Pb and this produces a well-defined linear regression. The end result is that the $^{207}Pb/^{206}Pb$ isotope composition of the common Pb component (y-intercept) is better constrained. This is the case for samples Oka203 and Oka206 (Fig. 6A–F). Moreover, the 'anchored' (*i.e.*, $^{207}Pb/^{206}Pb$ y-intercept value is fixed within IsoPlot) and 'unanchored' (free regression) yield identical radiogenic ages given their associated uncertainties. The linear regressions with an 'anchored' y-intercept value adopt a $^{207}Pb/^{206}Pb$ isotope ratio ~0.79 for the common Pb component based on the Pb isotope compositions of associated calcite (a mineral essentially devoid of U and Th) from Oka (Grünenfelder *et al.* 1986, Chen & Simonetti 2013). The corresponding weighted mean $^{206}Pb/^{238}U$ ages for niocalite from samples Oka203 and Oka206 are 110.6 ± 1.2 Ma and 115.0 ± 1.9 Ma, respectively (Fig. 6).

In the second scenario, the individual laser ablation analyses yield Pb/U isotope ratios that essentially overlap, *i.e.*, the proportions of 'radiogenic' and 'common' Pb are similar, which results in a cluster of points in the Tera-Wasserburg plot (Fig. 6G); hence, the Pb isotope composition of the common Pb component is more difficult to constrain in this situation (free regression), and 'anchoring' the linear regression through the y-intercept value of 0.79 (defined above) circumvents this issue. This is the case for sample Oka153 (Fig. 6G, H). The U/Pb isotope data for sample Oka153 indicates a slightly more complex situation, since a bimodal age distribution is defined in the Tera-Wasserburg plot (*i.e.*, more than one linear regression; Fig. 6G), and the corresponding weighted mean $^{206}Pb/^{238}U$ ages are 110.1 ± 5.0 Ma and 133.2 ± 6.1 Ma (Fig. 6H). A similar bimodal age distribution is also defined by apatite from the identical thin section of sample Oka153, with weighted mean $^{206}Pb/^{238}U$ ages of 111.4 ± 2.8 Ma and 126.9 ± 1.8 Ma (Chen & Simonetti 2013). The weighted mean $^{206}Pb/^{238}U$ crystallization ages for niocalite and apatite from their respective carbonatite samples are compared in Figure 7, and given their associated uncertainties, these indicate that niocalite and apatite co-crystallized.

In situ Sr isotopes

Strontium concentrations and isotopic ratios for niocalite are given in Table 3. The Rb/Sr ratios for most samples are extremely low, hence the minor correction for radiogenic in-growth of ^{87}Sr can be neglected. The *in situ* $^{87}Sr/^{86}Sr$ ratios range from 0.70314 to 0.70343, and values vary both within and amongst samples. The Sr isotope range recorded here overlaps that defined by ID-TIMS (0.70323 to 0.70333; Wen *et al.* 1987) for whole rock and mineral separates from Oka. Of note, however, is that the total variation in Sr isotope ratios documented here is slightly larger compared to the that reported by Wen *et al.* (1987).

DISCUSSION

Distribution of the trace elements

As described by Merlino & Perchiazzi (1988), the crystal structure of various minerals belonging to the

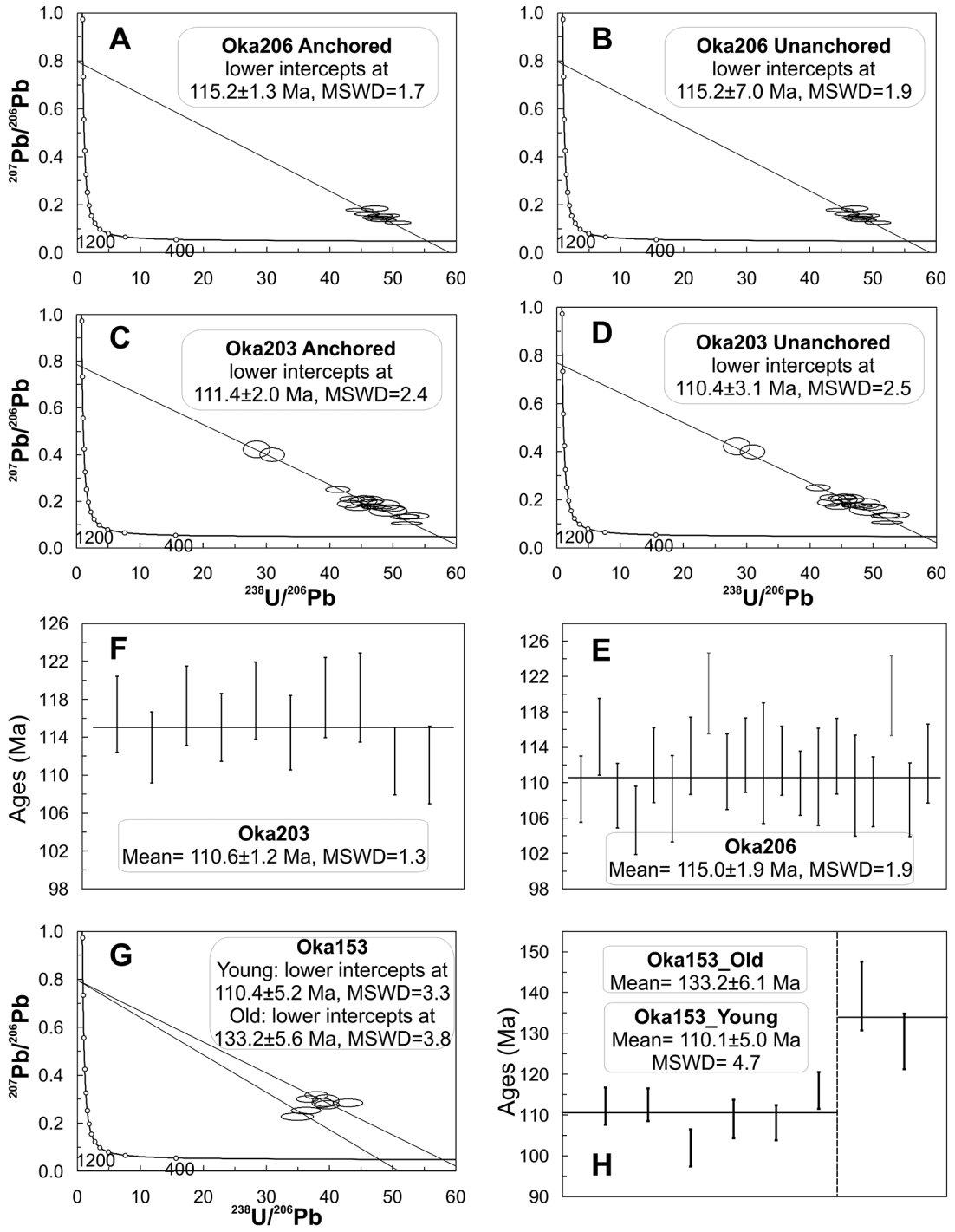

FIG. 6. Tera-Wasserburg plots (both 'anchored' and 'unanchored'- see text for details) and diagrams illustrating weighted mean $^{206}Pb/^{238}U$ ages for niocalite from samples Oka206 (A, B, E), Oka203 (C, D, F), and Oka153 (G, H). The two grayed analyses in diagram (E) are the rejected (at 2σ level) ages as determined by Isoplot version 3.0 (Ludwig 2003).

låvenite–cuspidine group differs because the diorthosilicate groups may be connected to the octahedral walls in different ways, *i.e.*, different cations may be located at different octahedral sites. On the basis of the major and trace element results reported in this study, most of the substitution schemes involving minor and trace cations are dictated by similar bond valences and effective ionic radii. For elements such as the REEs, Sr, and Ta that do not exert strong correlations with the major elements (*e.g.*, Ca), the exact substitution mechanism is relatively complex. However, their relative distribution could nonetheless be predicted via bond valence, and this is discussed below in relation to the REE abundances.

Fleet & Pan (1995) pointed out that the selectivity of REEs for Ca-bearing minerals is dependent on the size of the Ca-occupied lattice positions within individual crystal structures, *i.e.*, plagioclase is LREE-enriched due to large Ca-occupied octahedral lattice positions, minerals with medium-sized Ca positions (*e.g.*, clinopyroxene) are MREE-enriched, and phases with small Ca sites (*e.g.*, garnet) are HREE-enriched. Cuspidine is characterized by relatively small, bond-valence deficient Ca positions (Fleet & Pan 1995), thus such a mineral phase favors incorporation of the HREEs over the LREEs. According to Fleet & Pan (1995), trace elements favor different sites within the

TABLE 5. *IN SITU* U-Pb DATING RESULTS FOR NIOCALITE BY LA-ICP-MS

Sample	Analyses	Pb (ppm)	U (ppm)	^{206}Pb (cps)	^{207}Pb (cps)	^{238}U (cps)	^{207}Pb/^{206}Pb	2σ error	^{238}U/^{206}Pb	2σ error	F206	Rad. ^{206}Pb/^{238}U	Rad. ^{206}Pb/^{238}U Age (Ma)	2σ error
Oka206	T3	2.56	270	8875	1699	516401	0.13501	0.00454	48.51320	1.67288	0.12	0.01822	**116**	4
	T4	2.07	223	7572	1217	457654	0.12497	0.00557	50.79171	1.69141	0.10	0.01767	**113**	4
	T5	2.26	220	7855	973	443666	0.14087	0.00816	47.70960	1.70484	0.12	0.01837	**117**	4
	T9	1.96	252	6716	1129	394214	0.14456	0.00582	48.39525	1.50588	0.13	0.01800	**115**	4
	T10	2.55	185	7132	1001	389975	0.14563	0.00571	47.15032	1.62998	0.13	0.01845	**118**	4
	T11	2.41	235	6587	1014	376895	0.15388	0.00505	47.94027	1.65053	0.14	0.01792	**114**	4
	T12	2.08	281	6929	1000	368796	0.16053	0.00553	45.94000	1.63600	0.15	0.01850	**118**	4
	T17	2.27	175	4495	807	236288	0.17779	0.00525	44.68934	1.77775	0.17	0.01850	**118**	5
	T18	2.26	167	5399	831	313095	0.15469	0.00516	49.17876	1.57043	0.14	0.01744	**111**	4
	T19	2.60	252	4782	887	262111	0.18369	0.00858	47.12684	1.73914	0.18	0.01738	**111**	4
Oka203	NIO1	2.66	184	18034	2340	1105141	0.13366	0.00880	51.81478	1.77074	0.11	0.01710	**109**	4
	NIO2	3.71	455	8685	1823	439845	0.20883	0.01042	43.55816	1.64216	0.21	0.01803	**115**	4
	NIO3	3.23	685	12591	1715	780002	0.13497	0.00762	52.06510	1.75079	0.12	0.01698	**109**	4
	NIO4	2.26	645	15231	2021	954754	0.13717	0.01048	53.28719	1.94502	0.12	0.01654	**106**	4
	NIO5	2.61	561	8014	1543	421869	0.20172	0.01809	45.36500	1.70901	0.21	0.01752	**112**	4
	NIO6	2.34	861	9736	1708	580269	0.18355	0.01776	48.40297	2.18768	0.18	0.01692	**108**	5
	NIO7	2.61	729	20308	2110	1236931	0.10623	0.00456	52.15323	2.00831	0.08	0.01769	**113**	4
	NIO8	2.78	483	7974	1483	397498	0.18867	0.01261	43.20801	1.64368	0.19	0.01880	**120**	5
	NIO9	3.63	206	6947	3083	374547	0.20907	0.00749	45.10266	1.73083	0.21	0.01741	**111**	4
	NIO10	2.30	207	8376	1507	460477	0.18256	0.00468	46.35573	1.73085	0.18	0.01770	**113**	4
	NIO11	3.95	258	16256	7072	532825	0.42285	0.02897	28.42838	1.72756	0.50	0.01756	**112**	7
	NIO12	5.43	210	7068	1274	398109	0.17877	0.00701	46.90340	1.62235	0.17	0.01760	**112**	4
	NIO13	3.75	223	7800	1558	435475	0.19787	0.00744	46.51046	1.54297	0.20	0.01720	**110**	4
	NIO14	2.94	465	11389	1632	696818	0.15871	0.01860	49.23052	2.44487	0.15	0.01731	**111**	5
	NIO15	4.01	143	5969	1489	287517	0.25034	0.01012	41.28292	1.56060	0.27	0.01768	**113**	4
	NIO16	5.16	166	12811	5130	474798	0.39960	0.02347	30.90342	1.60785	0.47	0.01716	**110**	6
	NIO17	2.32	348	7320	1456	409688	0.20318	0.01518	46.51544	1.68309	0.21	0.01705	**109**	4
	NIO18	2.59	458	9833	1715	519010	0.17274	0.00971	44.43266	1.66662	0.17	0.01876	**120**	4
	NIO19	5.23	534	10145	1713	607872	0.17031	0.01088	49.50031	1.90312	0.16	0.01691	**108**	4
	NIO20	2.27	408	9763	1707	563104	0.17310	0.00448	47.47821	1.88806	0.17	0.01755	**112**	4
Oka153	NIO1	3.04	161	7597	2119	358986	0.27647	0.01397	39.58148	1.59315	0.31	0.01756	**112**	5
	NIO1_2	3.04	161	7091	2085	332596	0.28391	0.01526	38.89767	1.37813	0.32	0.01761	**113**	4
	NIO2	4.18	134	8109	2277	441519	0.28413	0.01295	42.94275	1.90740	0.32	0.01594	**102**	5
	NIO2_2	4.18	134	7064	2040	342370	0.29362	0.02003	39.40171	1.70565	0.33	0.01705	**109**	5
	NIO3	4.49	153	9855	2212	404983	0.22700	0.01266	34.87553	2.11188	0.24	0.02182	**139**	8
	NIO3_2	4.49	153	8858	2333	370743	0.25197	0.01133	36.26695	1.93866	0.27	0.02006	**128**	7
	NIO4	7.07	114	5670	1856	259896	0.31641	0.01204	37.92164	1.51222	0.36	0.01692	**108**	4
	NIO4_2	7.07	114	6293	1893	278229	0.30039	0.01073	36.48553	1.41122	0.34	0.01817	**116**	4

niocalite structure that are not completely bonded (*i.e.*, 'underbonded'). The bond valence and atomic distances of different Ca and Nb site(s) are reported in Table 4 and are based on data reported by Mellini (1982). The effective ionic radii for major and trace element cations present within niocalite are best explained by six-fold coordination (Shannon 1976; Table 6). The high field strength elements (*i.e.*, Ta, Ti) favor the Nb-occupied site on the basis of similar valence and effective ionic radii. Rare earth elements, Sr, and other cations with double valences favor the Ca sites. With the exception of the Ca(4) position, all the remaining lattice sites are variably underbonded, indicating the possibility for occupancy by other cations. The underbonded sites are also characterized by variable bond distances, and could host cations with different effective ionic radii. Strontium, with the largest effective ionic radius, prefers the Ca(6) and Ca(7) sites, since these possess the largest bond distances. The LREEs favor the second-largest Ca(1) and Ca(3) sites since the majority of the residual Ca(6) and Ca(7) sites are occupied by Sr. The Ca(2) and Ca(8) sites are characterized by the smallest bond distances and are therefore suitable for REEs, in particular the HREEs. Compared to the chondrite-normalized REE pattern and $(La/Yb)_N$ ratio for apatite from Oka (Fig. 5), niocalite contains higher contents of the HREEs. This can be attributed to the two Ca sites in apatite with bond distances that are both intermediate-to-large, such that the REE distribution within apatite results in a more negative chondrite-normalized REE pattern (Fig. 5). In contrast, the smaller Ca sites in niocalite preferentially incorporate the HREEs.

TABLE 6. EFFECTIVE IONIC RADII FOR MAJOR AND TRACE ELEMENT CATIONS IN SIX-FOLD COORDINATION (SHANNON 1976)

Cation	Six-fold ionic radius
Na^{+}	1.02
Ca^{2+}	1
Mn^{2+}	0.83
Fe^{2+}	0.78
Mg^{2+}	0.72
Ti^{4+}	0.605
Sr^{2+}	1.18
La^{3+}	1.032
Ce^{3+}	1.01
Pr^{3+}	0.99
Nd^{3+}	0.983
Sm^{3+}	0.958
Eu^{3+}	0.947
Gd^{3+}	0.938
Tb^{3+}	0.923
Dy^{3+}	0.912
Y^{3+}	0.9
Ho^{3+}	0.901
Er^{3+}	0.89
Tm^{3+}	0.88
Yb^{3+}	0.868
Lu^{3+}	0.861
Zr^{4+}	0.72
Hf^{4+}	0.71
Nb^{5+}	0.64
Ta^{5+}	0.64

Origin of niocalite

As summarized by Cox & Wilton (2006), geochronological results for the MIP-related alkaline intrusions define two age groups: 110–125 Ma and 125–140 Ma. This bimodal age distribution was also confirmed by the extensive *in situ* dating of apatite from various carbonatites and associated alkaline silicate rocks from the Oka carbonatite complex (Chen & Simonetti 2013). With the exception of two analyses for sample Oka153 (Fig. 6; Table 5), the majority of the niocalite ages (between ~110 and ~115 Ma) fall within the younger age group of the MIP (110–125 Ma). This result clearly indicates that most of the niocalite formed during the latter stages of melt differentiation and crystallization at the Oka complex. The two older niocalite ages overlap the older age group for apatite from the identical petrographic thin section, which clearly suggests simultaneous formation and a protracted crystallization history of niocalite in sample Oka153.

Kapustin (1980) proposed that niocalite typically forms during the early crystallization stage of phosphorus-free carbonatites. It is then ultimately replaced by lattrapite or pyrochlore, and possibly co-crystallizes with apatite during the crystallization of later (second stage) carbonatites. Alternatively, the formation of minerals belonging to the cuspidine–niocalite–baghdadite solid solution series in the metacarbonatites of the

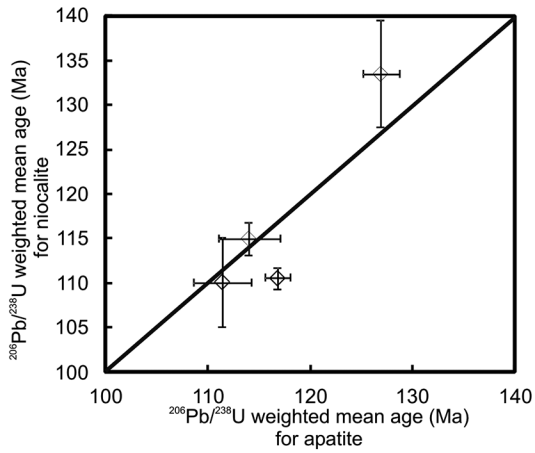

FIG. 7. $^{206}Pb/^{238}U$ weighted mean ages for niocalite *versus* those for corresponding apatite from the identical carbonatite host samples.

Basal Complex of Fuerteventura has been attributed to pyrochlore decarbonation (Casillas *et al*. 2008). The unbalanced reactions proposed by Casillas *et al*. (2008) are: $(Na,Ca)_2Nb_2O_6(OH,F)$ (pyrochlore) + $CaCO_3$ (calcite) + $CaSiO_3$ (wollastonite) + (F, H_2O; fluid phase) = $Ca_{16}(SiO_7)_4(F,OH)_8$ – $Ca_{14}Nb_2(Si_2O_7)_4O_6F_2$ (cuspidine–niocalite) + CO_2. Based on petrographic evidences for the carbonatite samples investigated here, it remains unclear whether niocalite is replaced by pyrochlore or vice versa. Back-scattered electron images (Fig. 2) indicate that pyrochlore occurs either as small crystals located at the edge of niocalite grains (Fig. 2E), or poorly shaped crystals located in fractures within niocalite grains (Fig. 2F). The latter textural feature supports Kapustin's (1980) model that niocalite is ultimately replaced by pyrocholore, and could possibly be accounted by the unbalanced reaction: $Ca_{14}Nb_2(Si_2O_7)_4O_6F_2$ (niocalite) + Fluid = $(Na, Ca)_2Nb_2O_6(OH, F)$ (pyrochlore) + $CaSiO_3$ (wollastonite).

With the exception of the two older ages identified for niocalite from sample Oka153, the remaining U-Pb ages are either similar (given their associated uncertainties) or slightly younger than those for apatite from the same sample (Fig. 7). Hence, niocalite formation at Oka involved a minor amount of crystallization during the earlier melt differentiation stage (~130 Ma), whereas the majority of the niocalite crystallized with apatite during the latter stages (~110–115 Ma) of the petrogenetic history of the complex. Ultimately, replacement of niocalite by pyrochlore may be attributed to late-stage hydrothermal activity as recorded by fluid inclusions within constituent minerals from the Oka complex (Samson *et al*. 1995).

An alternative model for niocalite formation was proposed by Mitchell & Belton (2004) based on its occurrence in natrocarbonatite lavas from Oldoinyo Lengai, Tanzania. Niocalite and associated minerals at Oldoinyo Lengai volcano may have formed via crystal fractionation, such that niocalite forms early and evolves to less Nb-rich compositions as indicated by textural relations (Mitchell & Belton 2004). On the basis of the U-Pb ages reported here, most of the niocalite crystallization occurred during the late stage of the magmatic evolution of the Oka carbonatite complex; this feature indicates that high activities of Nb and Si prevailed in the residual melt(s). The latter statement assumes, of course, that the carbonatites at Oka are petrogenetically related to a single parental melt. However, Chen & Simonetti (2013) clearly demonstrate that the magmatic activity at Oka was prolonged and spanned approximately 20 million years based on a detailed U-Pb geochronological investigation of apatite. Moreover, Chen & Simonetti (2013) also prove that the highly variable trace element compositions of apatite from Oka are difficult to reconcile with a closed system model involving fractional crystallization of a single parental carbonatite melt. Carbonatite samples (*e.g*., Oka153) containing both apatite and niocalite crystals that define a bimodal age distribution suggest that the older crystals were generated in earlier-formed, small-volume partial melts. These were then subsequently scavenged and incorporated by younger partial melts during their ascent and emplacement at crustal levels, and therefore the earlier-formed niocalite and apatite clearly represent cognate crystals.

The combined geochronological, major and trace element abundances, and Sr isotope results reported here do not define any correlations or trends relative to one another; hence, the entire set of analyses are difficult to reconcile with differentiation and crystallization processes associated with a single, parental carbonatite magma. In addition, the origin of the carbonatites and associated alkaline silicate rocks at Oka cannot be attributed to simple closed-system fractional crystallization, or liquid immiscibility involving a carbonated parental silicate melt, the main reason being that the $^{87}Sr/^{86}Sr$ isotope ratios (0.70314–0.70343) recorded by the niocalite grains are highly variable and consistent with open system behavior. The combined Sr isotope ratios and U-Pb ages for niocalite reported here strongly suggest, therefore, that the petrogenetic evolution of the Oka complex is rather complex. The lack of any correlations between chemical, isotopic, and geochronological data confirms this interpretation. Formation of the Oka complex most probably involved continuous partial melting of a heterogeneous mantle source over a ~20 Myr interval that yielded intermittent small volume melts. Although the latter are sampling a heterogeneous mantle source, the entire range of Sr isotope values (0.70314–0.70343) reported here are characteristic of derivation from a long-lived, time-integrated depleted source region. This finding was initially reported by Bell *et al*. (1982) on the basis of the depleted Sr isotope signatures for Canadian carbonatites spanning an age range between ~2.7 and 0.1 Ga; their study included the Sr isotope compositions for the Oka carbonatites. However, a chemical/physical mechanism at mantle depths is needed in order to produce the range in Sr isotope ratios recorded by the niocalite grains investigated here. One possibility is that mixing of mantle components has taken place between old, rigid continental lithosphere and underlying, convecting asthenospheric mantle. Lithosphere-asthenosphere mantle mixing has been proposed to explain the Nd-Sr-Pb isotope systematics of carbonatite complexes from East Africa, with the asthenospheric component linked to plume activity (*e.g*., Bell & Simonetti 1996, Bell & Simonetti 2010). Tectonic models put forward to explain the origin of the alkaline plutons belonging to the MIP involve melting of lithospheric mantle at the time of the opening of the North Atlantic Ocean (Faure *et al*. 1996), or of mantle plume origin (Eby 1985, Foland *et al*. 1988). The MIP has also been linked to the alkaline

intrusions of the Vermont White Mountains and the New England seamount chain as expressions of a hotspot track (Eby 1985, Foland *et al*. 1988). Therefore, it is possible that the variable Sr isotope values for niocalite record different degrees of lithosphere-asthenosphere (plume) interaction. The mechanism for producing isotopic heterogeneity within the continental lithosphere would involve periodic infiltration of more fertile, trace element-enriched CO_2-bearing melts/fluids that act as metasomatic agents (*e.g*., Bell & Simonetti 2010). Consequently, the final Sr isotope composition of the rock-forming minerals at Oka (calcite, apatite, niocalite) is a function of the degree of interaction between lithosphere and asthenospheric mantle components.

Conclusions

Niocalite is a calc-silicate niobate mineral belonging to the låvenite–cuspidine group, which preferentially incorporates double-valenced elements, REEs and HFSEs. On the basis of bond valences, HREE enrichment in niocalite (relative to coexisting apatite) is confirmed by the trace element abundances reported here.

This study reports for the first time *in situ* U-Pb dating results and Sr isotopes for niocalite from Oka, which indicates a complex and protracted petrogenetic history involving open magma-system behavior. The variable Sr isotope ratios and bimodal age distribution for niocalite suggest that the mantle source giving rise to the carbonatites and associated alkaline silicate rocks at Oka is heterogeneous (*i.e*., metasomatized), and the earlier-formed niocalite crystals represent cognate grains that are unrelated to their host carbonatite melt. A similar cumulate origin was previously proposed to explain the bimodal age distribution for apatites from Oka (Chen & Simonetti 2013).

Acknowledgements

We thank Dr. Ian Steele, University of Chicago Electron Microprobe Laboratory, for his assistance with data collection. The assistance provided by Dr. Ginger Sigmon with single crystal X-ray diffraction analysis at the Energy Frontier Research Center, University of Notre Dame is greatly appreciated.

References

Aarden, H.M. & Gittins, J. (1974) Hiortdahlite from Kipawa River, Villedieu Township, Temiscaming County, Quebec, Canada. *Canadian Mineralogist* **12**, 241–247.

Banerjee, N.R., Simonetti, A., Furnes, H., Muelenbachs, K., Staudigel, H., Heaman, L., & Van Kranendonk, M.J. (2007) Direct dating of Archean microbial ichnofossils. *Geology* **35**, 487–490.

Batumike, J.M., Griffin, W.L., Belousova, E.A., Pearson, N.J., O'Reilly, S.Y., & Shee, S.R. (2008) LAM-ICPMS U-Pb dating of kimberlitic perovskite: Eocene-Oligocene kimberlites from the Kundelungu Plateau, D.R. Congo. *Earth and Planetary Science Letters* **267**, 609–619.

Bell, K., Blenkinsop, J., Cole, T.J.S., & Menagh, D.P. (1982) Evidence from Sr isotopes for long-lived heterogeneities in the upper mantle. *Nature* **298**, 251–253.

Bell, K. & Simonetti, A. (1996) Carbonatite magmatism and plume activity: implications from the Nd, Pb and Sr isotope systematics of Oldoinyo Lengai. *Journal of Petrology* **37**, 1321–1339.

Bell, K. & Simonetti, A. (2010) Source of parental melts to carbonatites- critical isotopic constraints. *Mineralogy and Petrology* **98**, 77–89.

Bellezza, M., Merlino, S., & Perchiazzi, N. (2004) Chemical and structural study of the Zr, Ti-disilicates in the venanzite from Pian di Celle, Umbria, Italy. *European Journal of Mineralogy* **16**, 957–969.

Bizzarro, M., Simonetti, A., Stevenson, R.K., & Kurszlaukis, S. (2003) In situ $^{87}Sr/^{86}Sr$ investigation of igneous apatites and carbonates using laser ablation MC-ICP-MS. *Geochimica et Cosmochimica Acta* **67**, 289–302.

Casillas, R., Nagy, G., Demény, A., Ahijado, A., & Fernández, C. (2008) Cuspidine-niocalite-baghdadite solid solutions in the metacarbonatites of the Basal Complex of Fuerteventura (Canary Islands). *Lithos* **105**, 25–41.

Chakhmouradian, A.R., Mitchell, R.H., Burns, P.C., Mikhailova, Y., & Reguir, E.P. (2008) Marianoite, a new member of the cuspidine group from the Prairie Lake silicocarbonatite, Ontario. *Canadian Mineralogist* **46**, 1023–1032.

Chen, W. & Simonetti, A. (2013) In-situ determination of major and trace elements in calcite and apatite, and U-Pb ages of apatite from the Oka carbonatite complex: Insights into a complex crystallization history. *Chemical Geology* **353**, 151–172.

Chew, D.M., Sylvester, P.J., & Tubrett, M.N. (2011) U–Pb and Th–Pb dating of apatite by LA-ICP-MS. *Chemical Geology* **280**, 200–216.

Cox, R.A. & Wilton, D.H.C. (2006) U-Pb dating of perovskite by LA-ICP-MS: An example from the Oka carbonatite, Quebec, Canada. *Chemical Geology* **235**, 21–32.

Eby, G.N. (1984) Geochronology of the Monteregian Hills alkaline igneous province, Quebéc. *Geology* **12**, 468–470.

Eby, G.N. (1985) Age relations, chemistry, and petrogenesis of mafic alkaline dykes from the Monteregian Hills and younger White Mountain igneous provinces. *Canadian Journal of Earth Sciences* **22**, 1103–1111.

Faure, S., Tremblay, A., & Angelier, J. (1996) State of intraplate stress and tectonism of northeastern America

since Cretaceous times, with particular emphasis on the New England-Quebec igneous province. *Tectonophysics* **255**, 111–134.

Fleet, M.E. & Pan, Y. (1995) Crystal chemistry of rare earth elements in fluorapatite and some calc-silicates. *European Journal of Mineralogy* **7**, 591–605.

Fliegel, D., Kosler, J., Mcloughlin, N., Simonetti, A., De Wit, M.J., Wirth, R., & Furnes, H. (2010) In-situ dating of the Earth's oldest trace fossil at 3.34 Ga. *Earth Planetary Science Letters* **299**, 290–299.

Foland, K.A., Chen, J.F., Gilbbert, L.A., & Hofmann, A.W. (1988) Nd and Sr isotopic signatures of Mesozoic plutons in northeastern North America. *Geology* **16**, 684–687.

Foland, K.A., Gilbbert, I.A., Sebring, C.A., & Jiang-Feng, C. (1986) $^{40}Ar/^{39}Ar$ ages for plutons of the Monteregian Hills, Québec: evidence for a single episode of Cretaceous magmatism. *Geological Society of America Bulletin* **97**, 966–974.

Gold, D.P. (1972) The Monteregian Hills: ultra-alkaline rocks and the Oka carbonatite complex. *24th International Geology Congress Guidebook* **B–11**.

Gold, D.P., Eby, G.N., Bell, K., & Vallée, M. (1986) Carbonatites, diatremes and ultra-alkaline rocks in the Oka area, Quebec. *Geological Association of Canada Guidebook* **21**.

Grünenfelder, M., Tilton, G.R., Bell, K., & Blenkinsop, J. (1986) Lead and strontium isotope relationships in the Oka carbonatite complex, Québec. *Geochimica et Cosmochimica Acta* **50**, 461–468.

Horstwood, M.S.A., Foster, G.L., Parrish, R.R., Noble, S.R., & Nowell, G.M. (2003) Common-Pb corrected *in situ* U-Pb accessory mineral geochronology by LA-MC-ICP-MS. *Journal of Analytical Atomic Spectrometry* **18**, 837–846.

Kapustin, Y.L. (1980) *Mineralogy of Carbonatites*. Amerind Publishing Company, University of California, Berkley, U.S.A. .

Keller, J., Williams, C.T., & Koberski, U. (1995) Niocalite and wöhlerite from the alkaline and carbonatite rocks at Kaiserstuhl, Germany. *Mineralogical Magazine* **59**, 561–566.

Ludwig, K.R. (2003) ISOPLOT 3.0 – a geochronlogical tookit for Microsoft Excel. *Berkeley Geochronology Center Special Publication* **4**, 70.

Mcdonough, W.F. & Sun, S. (1995) The composition of the Earth. *Chemical Geology* **120**, 223–253.

Mellini, M. (1982) Niocalite revised: twining and crystal structure. *Tschermaks Mineralogische und Petrographische Mitteilungen* **30**, 249–266.

Merlino, S. & Perchiazzi, N. (1988) Modular mineralogy in the cuspidine group of minerals. *Canadian Mineralogist* **26**, 933–943.

Mitchell, R.H. & Belton, F. (2004) Niocalite-cuspidine solid solution and manganoan monticellite from natrocarbonatite, Oldoinyo Lengai, Tanzania. *Mineralogical Magazine* **68**, 787–799.

Nickel, E.H. (1956) Niocalite- a new calcium niobium silicate mineral. *American Mineralogist* **41**, 785–786.

Nickel, E.H., Rowland, J.F., & Maxwell, J.A. (1958) The composition and crystallography of niocalite. *Canadian Mineralogist* **6**, 264–272.

Paton, C., Woodhead, J.D., Hergt, J.M., Phillips, D., & Shee, S. (2007) Strontium isotope analysis of groundmass perovskite via LA-MC-ICP-MS. *Geostandards and Geoanalytical Research* **31**, 321–330.

Ramos, F.C., Wolf, J.A., & Tollstrup, D.L. (2004) Measuring $^{87}Sr/^{86}Sr$ variations in minerals and groundmass from basalts using LA-MC-ICP-MS. *Chemical Geology* **211**, 135–158.

Samson, I.M., Liu, W., & Williams-Jones, A.E. (1995) The nature of orthomagmatic hydrothermal fluids in the Oka carbonatite, Quebec, Canada: Evidence from fluid inclusions. *Geochimica et Cosmochimica Acta* **59**, 1963–1977.

Shannon, R.D. (1976) Revised effective ionic radii and systematic studies of interatomic distances in halides and chalcogenides. *Acta Crystallographica Section A* **32**, 751–767.

Simonetti, A., Heaman, L.M., & Chacko, T. (2008) Use of discrete-dynode secondary electron multipliers with Faradays – A 'reduced volume' approach for in-situ U-Pb dating of accessory minerals within petrographic thin section by LA-ICP-MS. *Goldschmidt Laser Ablation Short Course Volume* **40**, 241–264.

Simonetti, A., Heaman, L.M., Chacko, T., & Banerjee, N.R. (2006) In situ petrographic thin section U–Pb dating of zircon, monazite, and titanite using laser ablation–MC–ICP-MS. *International Journal of Mass Spectrometry* **253**, 87–97.

Simonetti, A., Heaman, L.M., Hartlaub, R.P., Creaser, R.A., Machattie, T.G., & Böhm C. (2005) U–Pb zircon dating by laser ablation-MC-ICP-MS using a new multiple ion counting Faraday collector array. *Journal of Analytical Atomic Spectrometry* **20**, 677–686.

Stern, R.A. & Amelin, Y. (2003) Assessment of errors in SIMS zircon U-Pb geochronology using a natural zircon standard and NIST SRM 610 glass. *Chemical Geology* **197**, 111–142.

Storey, C.D., Jeffries, T.E., & Smith, M. (2006) Common lead-corrected laser ablation ICP-MS U-Pb systematics and geochronology of titanite. *Chemical Geology* **227**, 37–52.

TAPPE, S. & SIMONETTI, A. (2012) Combined U-Pb geochronology and Sr-Nd isotope analysis of the Ice River perovskite standard, with implications for kimberlite and alkaline rock petrogenesis. *Chemical Geology* **304–305**, 10–17.

VAN ACHTERBERGH, E., RYAN, C.G., JACKSON, S.E., & GRIFFIN, W. (2001) Data reduction software for LA-ICP-MS. *In* Laser ablation-ICPMS in the earth science (P. Sylvester, ed.). *Mineralogical Association of Canada* **29**, 239–243.

WEN, J., BELL, K., & BLENKINSOP, J. (1987) Nd and Sr isotope systematics of the Oka complex, Quebec, and their bearing on the evolution of the sub-continental upper mantle. *Contributions to Mineralogy and Petrology* **97**, 433–437.

WU, F., YANG, Y., MITCHELL, R. H., LI, Q., YANG, J., & ZHANG, Y. (2010) In situ U-Pb age determination and Nd isotopic analysis of perovkites from kimberlites in southern Africa and Somerset Island, Canada. *Lithos* **115**, 205–222.

ZUREVINSKI, S.E. & MITCHELL, R.H. (2004) Extreme compositional variation of pyrochlore-group minerals at the Oka carbonatite complex, Quebec: evidence of magma mixing? *Canadian Mineralogist* **42**, 1159–1168.

Received December 13, 2013, revised manuscript accepted November 14, 2013.

APPENDIX

Mathematical approach for ^{207}Pb-age dating method

This method is based on the assumption that individual U-Pb analyses are concordant, and that any excess ^{206}Pb and ^{207}Pb is attributed to the common Pb component. This method utilizes the $^{207}Pb/^{206}Pb$ ratio for determining the relative amount of common Pb. The former can be obtained either by (1) equating it to the y-intercept of the best-fit linear regression as defined by individual analyses in the Tera-Wasserburg diagram; or (2) assume that the $^{207}Pb/^{206}Pb$ composition of the common Pb component is identical to that of coexisting U- and Th-free minerals (*e.g.*, calcite in our study). The proportion of common ^{206}Pb is then calculated as:

$$f_{206} = (^{207}Pb/^{206}Pb_{measured} - {}^{207}Pb^*/^{206}Pb^*) \,/\, (^{207}Pb^{206}Pb_{common} - {}^{207}Pb^*/^{206}Pb^*)$$

where the expected radiogenic $^{208}Pb^*/^{206}Pb^*$ ratio can be calculated from the estimated age (t; *i.e.*, from the Tera-Wasserburg diagram) by:

$$^{207}Pb^*/^{206}Pb^* = {}^{235}U/^{238}U[(e^{\lambda_{235}t} - 1)/(e^{\lambda_{238}t} - 1)] = 1/137.88[(e^{\lambda_{235}t} - 1)/(e^{\lambda_{238}t} - 1)$$

Radiogenic $^{206}Pb^*/^{238}U$ can then be calculated by:

$$^{206}Pb^*/^{238}U = (1 - f)(^{206}Pb/^{238}U_{measured})$$

Radiogenic age could be calculated by:

$$t = 1/\lambda_{238}\ln(^{206}Pb^*/^{238}U + 1)$$